Impact of Distal Mutation on Hydrogen Transfer Interface and Substrate Conformation in Soybean Lipoxygenase

Sarah J. Edwards, **Alexander V. Soudackov**, and **Sharon Hammes-Schiffer**
Department of Chemistry, 104 Chemistry Building, Pennsylvania State University, University Park, PA 16802

Sharon Hammes-Schiffer: shs@chem.psu.edu

Abstract

The impact of distal mutation on the hydrogen transfer interface properties and on the substrate mobility, conformation, and orientation in soybean lipoxygenase-1 (SLO) is examined. SLO catalyzes a hydrogen abstraction reaction that occurs by a proton-coupled electron transfer mechanism. Mutation of isoleucine 553 to less bulky residues has been found experimentally to increase the magnitude and temperature dependence of the kinetic isotope effect for this reaction. This residue borders the linoleic acid substrate but is ~15 Å from the active site iron. In the present study, we model these experimental data with a vibronically nonadiabatic theory and perform all-atom molecular dynamics simulations on the complete solvated wild-type and mutant enzymes. Our calculations indicate that the proton transfer equilibrium distance increases and the associated frequency decreases as residue 553 becomes less bulky. The molecular dynamics simulations illustrate that this mutation impacts the mobility, geometrical conformation, and orientation of the linoleic acid within the active site. In turn, these effects alter the proton donor-acceptor equilibrium distance and frequency, leading to the experimentally observed changes in the magnitude and temperature dependence of the kinetic isotope effect. This study provides insight into how the effects of distal mutations may be transmitted in enzymes to ultimately impact the catalytic rates.

I. Introduction

Lipoxygenases are non-heme metalloenzymes that catalyze the oxidation of fatty acids. Mammalian lipoxygenases are medically significant in terms of immune response[1] and cancer prevention.[2–5] Soybean lipoxygenase-1 (SLO) is often utilized as a model for mammalian lipoxygenases and has been studied extensively with a wide range of both experimental[6–14] and theoretical[13–30] methods. The reaction catalyzed by SLO is depicted in Figure 1. In the first step, the pro-*S* hydrogen from C11 of the natural substrate, linoleic acid, transfers to the Fe(III)-OH cofactor, forming a radical intermediate substrate and Fe(II)-OH$_2$. The radical intermediate substrate subsequently reacts with molecular oxygen to ultimately form hydroperoxyoctadecadienoic acid and Fe(III)-OH. The first step, which involves hydrogen abstraction, has been shown to be rate-limiting above 5 °C.[13,14] Moreover, quantum mechanical calculations,[20] as well as analysis of experimental measurements of thermodynamic quantities,[13,17] imply that the hydrogen abstraction occurs by a proton-coupled electron transfer (PCET) mechanism. In this mechanism, the electron transfers from the π-

system of the substrate to the iron of the cofactor, while the proton transfers from the C11 of the substrate to the hydroxyl ligand of the cofactor.

Kinetic studies of wild-type (WT) SLO indicate that the deuterium kinetic isotope effect (KIE) is unusually large,[7–10,13] with a value of 81 at room temperature, and that the temperature dependence of the catalytic rate constants and KIEs are relatively weak. These observations have been interpreted to imply a substantial degree of hydrogen tunneling with significant contributions from vibrational promoting modes that modulate the hydrogen tunneling distance.[13,17] Numerous SLO mutants have also been characterized structurally and kinetically.[11,13,14] Of particular interest is the mutation of the hydrophobic residue isoleucine 553 (I553) to leucine, valine, alanine, and glycine. As depicted in Figure 2, residue 553 borders the bound linoleic acid substrate but is ~15 Å from the active site iron. The experimental data show almost no structural changes due to these mutations but indicate that the magnitude and temperature dependence of the KIE increase as residue 553 becomes less bulky (i.e., along the series depicted in Figure 3).[14] These results have been interpreted to suggest an increased importance of donor-acceptor distance sampling as the size of the side chain at position 553 decreases.[14]

The SLO reaction has been studied with a broad spectrum of theoretical methods.[13–30] The experimental data have been analyzed in terms of various semiclassical and quantum mechanical rate models.[13–19] In addition, reduced models of the active site region have been studied with density functional theory[20–23] and mixed quantum/classical dynamical approaches.[24,25] Furthermore, the full enzymatic system has been studied with all-atom molecular dynamics simulations.[26–29] Olsson *et al.*[26,27] used an empirical valence bond potential energy surface to generate free energy profiles and included nuclear quantum effects with path integral methods. This work reproduced the magnitude but not the temperature dependence of the experimentally measured KIE for WT SLO. Tejero *et al.*[28] used a hybrid semiempirical quantum mechanical/molecular mechanical potential energy surface and ensemble-averaged variational transition state theory with multidimensional tunneling to calculate the rate constants for WT SLO and the I553A mutant. This work reproduced the magnitude of the KIE after applying a correction to the potential energy barrier but did not attempt to reproduce the temperature dependence. In these simulations, the proton donor-acceptor distance was observed to become larger and more flexible in the mutant reactant complex simulation.

Our previous molecular dynamics study of WT SLO[29] was based on a vibronically nonadiabatic theoretical formulation[31,32] that includes the quantum mechanical effects of the active electrons and the transferring proton, as well as the motions of all atoms in the entire solvated enzyme. In this theory, the rate constant is represented by the time integral of a probability flux correlation function. We performed classical molecular dynamics simulations of the complete solvated enzyme system to obtain the time correlation functions of the energy gap and the proton donor-acceptor mode, which were used to calculate the rate constant and KIE.[29] These calculations reproduced the experimentally observed magnitude and temperature dependence of the KIE for WT SLO without fitting any parameters directly to the experimental kinetic data. Furthermore, we found that the time-dependence of the probability flux correlation function is dominated by equilibrium properties, thereby validating the use of a simpler analytical rate constant expression for this system.

The objective of the present paper is to apply this vibronically nonadiabatic theoretical formulation to the series of I553 mutants of SLO in order to understand the impact of this distal mutation at a molecular level. We use a two-pronged approach to address this issue. In the first approach, we use the rate constant expressions derived within the framework of the vibronically nonadiabatic theory to model the experimental data for the WT and four mutant SLO enzymes.

This modeling provides insight into the fundamental physical principles underlying the experimentally observed trends in the magnitude and temperature dependence of the KIE upon mutation. Specifically, we find that relatively subtle changes in the proton donor-acceptor equilibrium distance and frequency lead to the experimentally observed trends. In the second approach, we perform all-atom classical molecular dynamics simulations of the entire solvated enzyme system for the WT and two mutant SLO enzymes. These simulations provide insight into how this distal mutation that borders the linoleic acid substrate but is ~15 Å from the active site iron could influence the properties of the proton transfer interface. In particular, we find that this mutation impacts the mobility, geometrical conformation, and orientation of the linoleic acid within the active site.

An outline of this paper is as follows. In Section II, we summarize the vibronically nonadiabatic theory and present the results obtained from modeling the experimental kinetic data for the WT and mutant SLO enzymes. In Section III, we describe the molecular dynamics methodology and present the analysis of the simulations for the WT and mutant SLO enzymes. In Section IV, we summarize the significant findings of this study and provide concluding remarks.

II. Modeling the Kinetic Data

A. Theory

In this paper, we model the experimental data using the vibronically nonadiabatic rate constant expressions derived previously.[31–33] In this formulation, the PCET reaction is described in terms of nonadiabatic transitions between pairs of reactant and product mixed electron-proton vibronic states. The nonadiabatic transitions are induced by thermal fluctuations of the solvent/protein environment, and these thermal fluctuations are assumed to occur on a much faster time scale than the nonadiabatic transitions. The vibronically nonadiabatic treatment is applicable to systems for which the nonadiabatic coupling between vibronic states is much less than the thermal energy. Our previous calculations indicate that the PCET reaction catalyzed by SLO is vibronically nonadiabatic.[17,29] In addition, the motion of the proton donor-acceptor distance R is treated explicitly, where M and Ω are the R-mode effective mass and frequency, respectively. The derivations of the nonadiabatic PCET rate constants are based on Fermi's golden rule and linear response theory for the solvent/protein environment.

In these derivations, the nonadiabatic coupling between reactant and product vibronic states is assumed to be of the form[34]

$$V_{\mu\nu}(R) = V_{\mu\nu}^{(0)} \exp\left[-\alpha_{\mu\nu}\left(R - \overline{R}_{\mu} \right) \right]$$

(1)

when R is near its equilibrium value $\overline{R}_{\mu}$. Here $V_{\mu\nu}^{(0)}$ is the vibronic coupling between vibronic states μ and ν at distance $R = \overline{R}_{\mu}$, and $\alpha_{\mu\nu}$ is the exponential decay parameter. This form of the coupling is a reasonable approximation in the region of R near its equilibrium value, as illustrated by expanding $\ln\left[V_{\mu\nu}/V_{\mu\nu}^{(0)} \right]$ in a Taylor series around $R = \overline{R}_{\mu}$ and retaining only the linear terms.[34] In the electronically nonadiabatic limit for proton transfer, Eq. (1) can be expressed as $V_{\mu\nu}(R) = V^{\mathrm{el}}S_{\mu\nu}(R)$, where V^{el} is the electronic coupling and $S_{\mu\nu}(R)$ is the overlap between the reactant and product proton vibrational wavefunctions for states μ and ν at a distance R.[35,36] In this limit, $V_{\mu\nu}^{(0)} = V^{\mathrm{el}}S_{\mu\nu}^{(0)}$, where $S_{\mu\nu}^{(0)}$ is the overlap at the distance $\overline{R}_{\mu}$, and the parameter $\alpha_{\mu\nu}$ describes the approximately exponential decay of the overlap with R near $\overline{R}_{\mu}$.

Using the short-time, high-temperature approximation for the solvent/protein environment and representing the R-mode as a quantum mechanical harmonic oscillator, the rate constant can be expressed as[31]

$$k^{\text{quant}}=\sum_{\mu}P_{\mu}\sum_{\nu}\frac{|V_{\mu\nu}^{(0)}|^2}{\hbar^2\Omega}\exp\left[\frac{2\lambda_{\mu\nu}^{(\alpha)}\zeta}{\hbar\Omega}\right]\int_{-\infty}^{\infty}d\tau\exp\left[-\frac{1}{2}\chi\tau^2+p(\cos\tau-1)+i(q\sin\tau+\theta\tau)\right]$$

(2)

with the dimensionless parameters defined as

$$\zeta=\coth(\tfrac{1}{2}\beta\hbar\Omega);\ \chi=\frac{2\lambda}{\beta\hbar^2\Omega^2};\ \theta=\frac{\Delta G_{\mu\nu}^0+\lambda}{\hbar\Omega}$$
$$p=\zeta\frac{\lambda_{\mu\nu}^{(\alpha)}}{\hbar\Omega};\ q=\frac{\lambda_{\mu\nu}^{(\alpha)}}{\hbar\Omega}$$

(3)

In this expression, the summations are over reactant states μ and product states ν, P_{μ} is the Boltzmann probability for reactant state μ, $\Delta G_{\mu\nu}^0$ is the free energy of reaction for states μ and ν, λ is the reorganization energy, $\lambda_{\mu\nu}^{(\alpha)}=\hbar^2\alpha_{\mu\nu}^2/2M$, and $\beta=1/k_{\text{B}}T$. This short-time, high-temperature approximation for the solvent/protein environment is valid when λ is large enough to ensure that the solvent/protein fluctuation dynamics are fast relative to the coherent nonadiabatic transitions. This expression also assumes that the reorganization energy and equilibrium proton donor-acceptor distance are the same for all pairs of reactant and product vibronic states.

The rate constant given in Eq. (2) can be further simplified in the high-temperature (low-frequency) regime for the R-mode, where $\hbar\Omega\ll k_{\text{B}}T$. In this regime, the rate constant has the form[31,32]

$$k^{\text{highT}}=\sum_{\mu}P_{\mu}\sum_{\nu}\frac{|V_{\mu\nu}^{(0)}|^2}{\hbar}\exp\left[\frac{2k_{\text{B}}T\alpha_{\mu\nu}^2}{M\Omega^2}\right]\sqrt{\frac{\pi}{\left(\lambda+\lambda_{\mu\nu}^{(\alpha)}\right)k_{\text{B}}T}}\exp\left[-\frac{\left(\Delta G_{\mu\nu}^0+\lambda+\lambda_{\mu\nu}^{(\alpha)}\right)^2}{4\left(\lambda+\lambda_{\mu\nu}^{(\alpha)}\right)k_{\text{B}}T}\right].$$

(4)

This expression is derived by performing a short-time expansion of the trigonometric functions in Eq. (2) up to second order and evaluating the time integral analytically. Eq. (4) leads to a simplified expression for the KIE when the reorganization energy and driving force are independent of isotope, $\lambda_{\mu\nu}^{(\alpha)}\ll\ll\lambda$, and only the ground reactant and product vibronic states contribute to the rates. Under these conditions,[29]

$$\text{KIE}\approx\frac{|S_{\text{H}}|^2}{|S_{\text{D}}|^2}\exp\left[-\frac{2k_{\text{B}}T}{M\Omega^2}\left(\alpha_{\text{D}}^2-\alpha_{\text{H}}^2\right)\right]$$

(5)

and

$$\frac{d}{dT}\ln[\text{KIE}] \approx -\frac{2k_B}{M\Omega^2}\left(\alpha_D^2 - \alpha_H^2\right).$$

(6)

Here S_H and S_D are the overlaps of the hydrogen and deuterium ground state wavefunctions, and α_H and α_D describe the approximately exponential dependence of these overlaps on R. In the application to SLO described below, we calculate the KIEs using both Eqs. (2) and (4), converging the results with respect to the excited reactant and product vibronic states. The simplified forms for the KIE and its temperature dependence given in Eqs. (5) and (6) are used only to analyze the physical principles dictating the qualitative trends.

An alternative rate constant expression attributed to Kutznetsov and Ulstrup[37] has been applied to SLO by Klinman and coworkers.[13,14,30,38] This expression is of the form

$$k^{\text{UK}} = \sum_\mu P_\mu \sum_\nu \frac{|V^{\text{el}}|^2}{\hbar} \sqrt{\frac{\pi}{\lambda k_B T}} \exp\left[-\frac{(\Delta G_{\mu\nu}^0 + \lambda)^2}{4\lambda k_B T}\right] \int_0^\infty P(R)\left[S_{\mu\nu}(R)\right]^2 dR$$

(7)

where $P(R) = \sqrt{\dfrac{M\Omega^2}{2\pi k_B T}} \exp\left[-M\Omega^2(R - \overline{R})^2/(2k_B T)\right]$ is the Boltzmann probability for a classical harmonic oscillator representation of the R-mode. In principle, the harmonic approximation for the R-mode could be avoided by using a more realistic probability distribution $P(R)$. Note that the integration limits are chosen differently in some implementations, but $P(R)$ and therefore the integrand are negligible for values of R deviating significantly from $R = \overline{R}$. Similar to the other rate constant expressions given above, this expression relies on Fermi's golden rule formalism and linear response theory for the solvent/protein environment. In addition, this expression is based on the assumptions that the proton vibrational motion is in the low-temperature (high-frequency) regime, the proton motion is not coupled to the solvent, and the R-mode is in the high-temperature (low-frequency) regime.[39–41] The rate constants k^{UK} and k^{highT} become identical when the following three conditions are satisfied: the proton transfer is electronically nonadiabatic (i.e., $V_{\mu\nu} = V^{\text{el}}S_{\mu\nu}$), the overlap decreases exponentially with R near its equilibrium value (i.e., $S_{\mu\nu} = S_{\mu\nu}^{(0)}\exp\left[-\alpha_{\mu\nu}(R - \overline{R}_\mu)\right]$), and $\lambda_{\mu\nu}^{(\alpha)} \ll\ll \lambda$.[42] Both k^{UK} and k^{highT} are only strictly valid in the low-frequency regime for the R-mode, where $\hbar\Omega < k_B T$, but k^{quant} given in Eq. (2) is valid for general R-mode frequencies. A detailed comparison of these expressions for a series of model systems has been presented elsewhere.[43]

B. Results of Modeling

We used the vibronically nonadiabatic theory of PCET described above to model the experimental kinetic data for the series of I553 mutants of SLO. For the purposes of this modeling study, the solvent reorganization energy is 39 kcal/mol, as calculated previously from molecular dynamics simulations of WT SLO, and the driving force is −5.4 kcal/mol, as estimated previously on the basis of experimental data.[29] The reactant and product proton potential energy curves are described by Morse potentials corresponding to a C–H and O–H vibrational mode, respectively, with the parameters given in Ref. [29]. The Morse potentials are positioned so that the minima of the reactant and product potentials are separated by a distance of $\overline{R} - R_{\text{CH}}^0 - R_{\text{OH}}^0$, where R_{CH}^0 and R_{OH}^0 correspond to the equilibrium C–H and O–H bond lengths of 1.09 and 0.96 Å, respectively. The hydrogen and deuterium vibrational wavefunctions are calculated by solving a one-dimensional Schrödinger equation for the hydrogen or deuterium moving in the reactant and product Morse potentials. Analytical solutions are available for the

eigenfunctions of Morse potentials.[44] The overlaps $S_{\mu\nu}^{(0)}$ between the reactant and product vibrational wavefunctions at $\bar{R}$ are calculated numerically. The parameters $\alpha_{\mu\nu}$ are determined for each pair of vibronic states by calculating the numerical derivatives of the natural logarithm of the corresponding overlap integrals with respect to R at $\bar{R}$. Note that a three-dimensional description of the hydrogen vibrational wavefunction with a more realistic proton potential would impact the quantitative results of this modeling study but is not expected to alter the qualitative trends. The value of V^{el} is assumed to be isotopically independent and therefore is not required for the calculation of the KIE.

For each SLO mutant, we determined the values of the equilibrium proton donor-acceptor distance, $\bar{R}$, and the effective R-mode frequency, Ω by minimizing the root-mean-square deviation (RMSD) between the calculated and experimental values for the ln[KIE]. Thus, we minimized the function

$$\chi = \sqrt{\sum_{i=1}^{N} (\ln[\,KIE_{calc}(T_i)] - \ln[\,KIE_{expt}(T_i)])^2},$$

where N is the number of experimental data points, T_i is the temperature for data point i, and KIE_{calc} and KIE_{expt} are the calculated and experimental KIEs, respectively. The values of KIE_{calc} were determined using both k^{quant} and k^{highT}. The values of $\bar{R}$ and Ω obtained from this fitting procedure are given in Table 1. To generate these results, the effective R-mode mass M was chosen to be 100 amu, as used in previous modeling studies.[43] The results with two other masses, as well as a brief discussion of the impact of the mass M on the results, are given in Supporting Information. The qualitative trends are the same for all three values of the masses.

Figure 4 depicts the experimental data points and the curves calculated using the rate constant k^{quant} with values of $\bar{R}$ and Ω given in Table 1. As shown in Figure 4, the magnitude and temperature dependence of the KIE increases as residue 553 becomes less bulky. Moreover, Table 1 indicates that the proton donor-acceptor equilibrium distance increases and the proton donor-acceptor mode frequency decreases as residue 553 becomes less bulky. Note that this trend is not followed by I553L and I553A because the experimental data for these two mutants are so similar that the theoretical modeling is unable to distinguish between them. Table 1 also shows that similar results are obtained with both k^{quant} and k^{highT}, thereby indicating that this system is in the low-frequency R-mode regime for these parameters. We emphasize that the specific values of $\bar{R}$ and Ω obtained from this procedure are not directly related to experimentally measurable quantities due to the approximate nature of the model. Moreover, as discussed in Supporting Information, the magnitude of the frequency Ω depends on the choice of the associated mass M. On the other hand, the trends in these effective distances and frequencies provide useful mechanistic insights, as well as predictions concerning the impact of mutation on the KIE.

The correlation between the changes in proton donor-acceptor equilibrium distance and frequency and the magnitude and temperature dependence of the KIE can be analyzed in terms of the simplified expressions given in Eqs. (5) and (6). As indicated by Eq. (5), the magnitude of the KIE will increase as the ratio of the hydrogen to deuterium overlaps increases. In general, this ratio increases as the equilibrium proton donor-acceptor distance increases.[32] Thus, if all other quantities remain the same, the magnitude of the KIE is expected to increase as $\bar{R}$ increases, as observed in Figure 4 and Table 1. As shown in Table 1, however, the frequency decreases as the equilibrium proton donor-acceptor distance increases. Eq. (5) indicates that the magnitude of the KIE will decrease as the frequency Ω decreases, so these two effects

impact the KIE in opposite directions. For this system, the increase in the equilibrium proton donor-acceptor distance dominates over the decrease in the frequency, but the magnitude of the KIE for the mutants is moderated by these opposing factors. In addition, Eq. (6) indicates that the temperature dependence of ln[KIE] will increase as the frequency Ω decreases, as observed in Figure 4 and Table 1.

Klinman and coworkers observed similar trends using k^{UK}, but their equilibrium distances were significantly higher and frequencies were significantly lower.[14,45] Specifically, they found that $\bar{R}$ increases from 3.29 Å to 4.60 Å and Ω decreases from 64 cm^{-1} to 38 cm^{-1} over the series of mutants spanning I553V to I553G. They used a similar effective mass of $M = 110$ amu, reorganization energy of $\lambda = 19$ kcal/mol, driving force of $\Delta G^0 = -6.0$ kcal/mol, and similar Morse parameters for the proton potentials. Using k^{highT} with the exact same parameters as used by Klinman and coworkers, we obtained virtually identical values for $\bar{R}$ and Ω as given in Table 1 and similar level of agreement with the experimental data as shown in Figure 4. These results are given in Supporting Information. Thus, the discrepancies in the values of $\bar{R}$ and Ω do not arise from differences in the other parameters. Using k^{UK}, we found that multiple combinations of $\bar{R}$ and Ω lead to reasonable agreement with the experimental data and that the specific values obtained depend on the details of the fitting procedure. In other words, the surface generated by plotting χ as a function of $\bar{R}$ and Ω is relatively flat in this regime. Note that the expressions k^{highT} and k^{quant} are not valid for the very low frequencies obtained by Klinman and coworkers because the approximation that the overlap between the reactant and product proton vibrational wavefunctions decreases exponentially with R in the relevant regime near the equilibrium distance $\bar{R}$ becomes invalid for such low frequencies. Moreover, the expression k^{UK} is also not reliable for very large equilibrium distances and low frequencies due to the anharmonicity of the proton donor-acceptor mode and numerical difficulties arising from the extremely small overlap integrals in this regime. As a result, the fitting procedure is more robust with k^{highT} and k^{quant} than with k^{UK}. In any case, the general trends observed in the two studies are in complete agreement.

III. Molecular Dynamics Simulations

A. Computational Methods

In order to elucidate the molecular basis for the trends described in the previous section, we performed molecular dynamics simulations for the WT SLO and the I553A and I553G mutants. The initial coordinates for the WT SLO were obtained from the X-ray crystallographic structure (PDB code 1YGE).[6] The simulations for the I553A and I553G mutants were each performed with two different initial structures. The first pair of initial structures was based on the X-ray crystallographic structure of wild-type SLO (PDB code 1YGE),[6] and the profix utility in the JACKAL protein modeling package[46,47] was used to perform the I553A or I553G mutation. The second pair of initial structures was based on the X-ray crystallographic structures of the I553A and I553G mutants (PDB codes 3BNE and 3BNC, respectively),[14] where the unresolved residues were added with the profix utility in JACKAL.[46,47] These initial structures are denoted Structure 1 and Structure 2, respectively, for each mutant. The root-mean-square deviation (RMSD) between the backbone residues of Structure 1 and Structure 2 was calculated with the VMD program[48] to be 1.73 Å for the I553A mutant and 0.97 Å for the I553G mutant. Performing the MD simulations with two different starting structures allowed us to analyze the sensitivity of the results to the starting structure. The H++ database[49,50] was used to determine the protonation states of the residues in the enzyme. The enzyme was solvated in a periodically replicated truncated octahedral box with dimensions of $110 \times 110 \times 110$ Å with ~18,000 explicit TIP3P[51−53] water molecules. To neutralize the overall charge of the system, peripheral water molecules were replaced with sodium cations.

Currently a crystal structure of SLO with bound linoleic acid substrate is not available, leading to uncertainty about the positioning of the substrate during catalysis. We obtained the initial conformation of the linoleic acid substrate for our simulations from previous quantum mechanical and docking calculations.[29] This conformation is in the reverse orientation compared to that postulated on the basis of experimental kinetic studies.[12] On the other hand, the orientation we are using is consistent with the orientation determined crystallographically for the purple form of soybean lipoxygenase-3 with bound product (PDB 1IK3).[54] It is also consistent with the orientation used for the simulations in Ref. [28], where the active sites of the two lipoxygenase structures[6,54] were overlapped, and the product was transformed to linoleic acid by superimposing the common atoms. Furthermore, a number of experiments on lipoxygenases suggest that the substrate could bind in both orientations.[55] These issues are directions for future study.

We performed the molecular dynamics simulations with a modified version of DLPROTEIN.[56,57] The potential energy surface was based on the AMBER 99 forcefield[53] with modifications described in Ref. [29] to describe the linoleic acid substrate and Fe cofactor. The entire solvated enzyme system, which consists of ~67,000 atoms, was allowed to move during the molecular dynamics simulations. Long-range electrostatic interactions were calculated with the Smooth Particle Mesh Ewald method.[58] All bonds involving hydrogen were constrained to their equilibrium lengths with the SHAKE algorithm.[59] The classical equations of motion were integrated with the velocity Verlet algorithm[60] with a time step of 1 fs. The NPT and NVT simulations were both performed with Nosé-Hoover thermostats.[61,62]

Each system was thoroughly equilibrated prior to data collection. To prevent the linoleic acid substrate from dissociating, the distance between C11 of the linoleic acid substrate and the oxygen of the hydroxyl ligand was constrained to 3.2 Å, the sum of the van der Waals radii of carbon and oxygen, during equilibration. Initially, the energy of the entire system was minimized in a three step procedure: (1) the solvent water molecules were optimized while the entire enzyme was fixed; (2) the mutated or added residues were optimized while the rest of the enzyme was fixed; (3) the entire system, including the enzyme, substrate, and solvent molecules, was optimized. Subsequently, molecular dynamics trajectories were propagated for 50 ps at 100, 200, and 300K with the NPT ensemble. In the final phase of equilibration, molecular dynamics trajectories were propagated for 100 ps at 300K with the NVT ensemble.

The data collection for each initial structure consisted of three parallel molecular dynamics trajectories with different initial velocities. These simulations were performed at 303 K for 1 ns starting from Structures 1 and 2 of the I553A and I553G mutants, as well as the WT structure used in previous studies, yielding a total of 3 ns of data for each of the five initial structures. In order to prevent substrate dissociation, the proton donor-acceptor distance was constrained to 2.72 Å in the WT SLO, 2.83 Å in the I553A mutant, and 2.96 Å in the I553G mutant. These values were determined from the modeling of the kinetic data described in Section II. Although these constraints may impact the results, they were necessary to prevent substrate dissociation over the relatively long nanosecond time scales of the MD trajectories. Our analysis focuses on properties that are not expected to be directly impacted by this constraint.

B. Molecular Dynamics Results

We analyzed the mobility, geometrical conformation, and orientation of the linoleic acid substrate in the active site of the WT and mutant enzymes. For the purposes of analysis, we divide linoleic acid into three regions, as depicted in Figure 2. Region I consists of backbone carbons 1 through 8, Region II consists of backbone carbons 9 through 13, and Region III consists of backbone carbons 14 through 18. As illustrated in Figure 2, the proton donor carbon 11 is contained in Region II, and the mutation site 553 is closest to Region I. For completeness, we present the data obtained with both initial structures for each mutant, where Structure 1

corresponds to the mutated WT crystal structure, and Structure 2 corresponds to the crystal structure of the mutant. The data from Structures 1 are biased toward the initial WT structure and hence may not provide a reliable representation of the mutant enzymes. In many cases, the results obtained with both initial structures are qualitatively similar, but when they differ, we focus our analysis mainly on the data obtained from Structures 2.

We analyzed the root-mean-square fluctuation (RMSF) of the linoleic acid backbone atoms to examine the substrate flexibility and motion. For this purpose, we aligned the active site residues, without including the linoleic acid substrate itself, of all configurations from each set of molecular dynamics trajectories. The active site was defined to include all residues with at least one atom within 5 Å of the linoleic acid in the initial WT structure, as well as the Fe cofactor with ligands. The residues included in the active site are: GLU 256, THR 259, LYS 260, VAL 354, SER 491, HID 494, GLN 495, HID 499, TRP 500, HID 504, ILE 538, LEU 541, ALA 542, SER 545, LEU 546, ILE 552, ILE/ALA/GLY 553, THR 556, PHE 557, HID 690, ASN 694, GLN 697, THR 709, SER 747, VAL 750, ILE 751, LEU 754, ILE 839. Elimination of the linoleic acid substrate in the alignment procedure allowed us to analyze the motion of the substrate within the active site.

Figure 5 depicts the RMSF of the linoleic acid backbone carbon atoms. This figure indicates that Region II is less mobile than Regions I or III. The smaller mobility of Region II is due to several factors, including the restrictions associated with being located in the middle of the molecule, the π-bonding in this region, and the constraint applied to the distance between the substrate C11 and the oxygen of the hydroxyl ligand on the iron cofactor. A comparison between Figures 5a and 5b indicates that the RMSFs for the two different initial structures for each mutant are similar in Regions I and II but are different in Region III. In both figures, the substrate motions are qualitatively similar for the WT and mutants in Regions I and II, and the substrate fluctuations are greater in Region I than in Region II. According to the more reliable Figure 5b, the substrate is significantly more mobile in Region III for WT than for the two mutants, suggesting a possible allosteric effect of the I553 mutation on the substrate motion, although the physical basis for this effect is unclear.

In addition to analyzing the substrate RMSFs, we also analyzed the thermally averaged distances between the backbone carbons at the ends of Regions I, II, and III. These thermally averaged distances, along with the standard deviations, are depicted in Figure 6. The observed trends are not indicative of changes in carbon-carbon bond distances, which are maintained by harmonic potentials, but rather represent more global conformational changes in the linoleic acid substrate backbone. The standard deviations in Figure 6 are consistent with Figure 5 in that Region I exhibits the greatest deviation and Region II exhibits the smallest deviation.

Figure 6 illustrates the changes in the average end-to-end distances of the three regions as residue 553 becomes less bulky. Regions I and III do not exhibit clear trends. In Region II, however, the C9–C13 distance exhibits a distinct increase as I553 becomes less bulky. Although the increase in this average distance is of similar magnitude as the RMSF in this region, the trend appears to be meaningful based on the standard deviations provided in Figure 6. This increase in the C9–C13 distance indicates a stretching of the linoleic acid backbone in Region II that could lead to an increase in the proton donor-acceptor distance between C11 and the hydroxyl oxygen. These molecular dynamics simulations do not provide any information about causal effects, but the modeling in the previous section suggests that the stretching of the linoleic acid backbone in Region II is correlated with the increase in the proton donor-acceptor distance.

We also calculated the thermally averaged distances between the linoleic acid backbone carbon atoms and the α-carbon of residue 553. These distances are depicted in Figure 7. This figure

suggests that the placement and orientation of the substrate within the active site changes upon mutation of I553. The linoleic acid backbone carbon closest to the α-carbon of residue 553 is C3 in WT and is shifted to C5 in both mutants for the initial Structures 2 and to an even higher-numbered substrate carbon in both mutants for the initial Structures 1. As implied by Figure 2, this shifting of the substrate relative to residue 553 is consistent with an increase in the equilibrium proton donor-acceptor distance upon mutation. Figure 7 also indicates that the substrate is closer to the α-carbon of residue 553 for the I553G mutant than for the I553A mutant. This trend is consistent with a larger equilibrium proton donor-acceptor distance for the less bulky residue glycine than for alanine. Thus, this analysis suggests that mutation at residue 553 may lead to re-orientation of the substrate in the active site.

V. Summary and concluding remarks

In this paper, we examined the impact of distal mutation on the hydrogen transfer interface properties and on the substrate mobility, conformation, and orientation in SLO. This study is based on experimental data showing that the magnitude and temperature dependence of the KIE increase as the distal residue 553 becomes less bulky. Modeling of this experimental data with a vibronically nonadiabatic theory indicates that the proton transfer equilibrium distance increases and the associated frequency decreases as residue 553 becomes less bulky. Molecular dynamics simulations of the complete solvated enzyme for WT and mutant SLO enzymes provide insight into how this distal mutation could affect these properties of the proton transfer interface. The simulations suggest that the replacement of I553 with a less bulky residue may lead to a decrease in the mobility of the opposite end of the substrate and a stretching of the middle region of the substrate backbone, which includes the proton donating carbon atom. Furthermore, the simulations also suggest a shifting of the substrate relative to residue 553 upon mutation of this residue, as well as a movement of the substrate closer to residue 553 as this residue becomes less bulky. These changes in mobility, conformation, and orientation of the substrate are correlated with the increase in the proton donor-acceptor equilibrium distance and decrease in the associated frequency. Distinguishing between cause and effect, however, is not possible due to limitations of the MD simulations.

The insights that have been generated from the vast body of experimental and theoretical studies of SLO have implications beyond this specific system. In general, distal mutations have been observed to significantly impact catalytic rates for many enzymes. Such effects are particularly apparent for reactions involving hydrogen tunneling, which is extremely sensitive to the proton donor-acceptor distance and frequency. For these types of reactions, measurement of the magnitude and temperature dependence of the KIE provides an exquisitely sensitive probe of the impact of mutation. A combination of structural and kinetic studies, in conjunction with theoretical modeling and computer simulations, will continue to enhance our understanding of how the effects of mutations are transmitted through proteins to ultimately impact the catalytic rates.

Supplementary Material

Refer to Web version on PubMed Central for supplementary material.

Acknowledgments

References

1. Samuelsson B, Dahlen SE, Lindgren JA, Rouzer CA, Serhan CN. Science 1987;237:1171. [PubMed: 2820055]

2. Steele VE, Holmes CA, Hawk ET, Kopelovich L, Lubet RA, Crowell JA, Sigman CC, Kelloff GJ. Cancer, Epidemiology, Biomarkers, & Prevention 1999;8:467.

3. Rioux N, Castonguay A. Carcinogenesis 1998;19:1393. [PubMed: 9744535]

4. Nie D, Hillman GG, Geddes T, Tang K, Pierson C, Grignon DJ, Honn KV. Cancer Research 1998;58:4047. [PubMed: 9751607]

5. Ghosh J, Myers CE. Proc Natl Acad Sci USA 1998;95:13182. [PubMed: 9789062]

6. Minor W, Steczko J, Stec B, Otwinowski Z, Bolin JT, Walter R, Axelrod B. Biochemistry 1996;35:10687. [PubMed: 8718858]

7. Glickman MH, Wiseman JS, Klinman JP. Journal of the American Chemical Society 1994;116:793.

8. Hwang CC, Grissom CB. Journal of the American Chemical Society 1994;116:795.

9. Jonsson T, Glickman MH, Sun S, Klinman JP. Journal of the American Chemical Society 1996;118:10319.

10. Rickert KW, Klinman JP. Biochemistry 1999;38:12218. [PubMed: 10493789]

11. Tomchick DR, Phan P, Cymborowski M, Minor W, Holman TR. Biochemistry 2001;40:7509. [PubMed: 11412104]

12. Knapp MJ, Seebeck FP, Klinman JP. Journal of the American Chemical Society 2001;123:2931. [PubMed: 11457000]

13. Knapp MJ, Rickert KW, Klinman JP. Journal of the American Chemical Society 2002;124:3865. [PubMed: 11942823]

14. Meyer MP, Tomchick DR, Klinman JP. Proceedings of the National Academy of Sciences (USA) 2008;105:1146.

15. Kuznetsov AM, Ulstrup J. Canadian Journal of Chemistry 1999;77:1085.

16. Knapp MJ, Klinman JP. European Journal of Biochemistry 2002;269:3113. [PubMed: 12084051]

17. Hatcher E, Soudackov AV, Hammes-Schiffer S. Journal of the American Chemical Society 2004;126:5763. [PubMed: 15125669]

18. Mincer JS, Schwartz SD. Journal of Chemical Physics 2004;120:7755. [PubMed: 15267689]

19. Siebrand W, Smedarchina Z. Journal of Physical Chemistry B 2004;108:4185.

20. Lehnert N, Solomon EI. J Biol Inorg Chem 2003;8:294. [PubMed: 12589565]

21. Borowski T, Krol M, Chruszcz M, Broclawik E. Journal of Physical Chemistry B 2001;105:12212.

22. Borowski T, Broclawik E. Journal of Physical Chemistry B 2003;107:4639.

23. Tejero I, Eriksson LA, Gonzalez-Lafont A, Marquet J, Lluch JM. Journal of Physical Chemistry B 2004;108:13831.

24. Tresadern G, McNamara JP, Mohr M, Wang H, Burton NA, Hillier IH. Chemical Physics Letters 2002;358:489.

25. Iyengar SS, Summer I, Jakowski J. Journal of Physical Chemistry B 2008;112:7601.

26. Olsson MHM, Siegbahn PEM, Warshel A. Journal of Biological Inorganic Chemistry 2004;9:96. [PubMed: 14663649]

27. Olsson MHM, Siegbahn PEM, Warshel A. Journal of the American Chemical Society 2004;126:2820. [PubMed: 14995199]

28. Tejero I, Garcia-Viloca M, Gonzalez-Lafont A, Lluch JM, York DM. Journal of Physical Chemistry B 2006;110:24708.

29. Hatcher E, Soudackov AV, Hammes-Schiffer S. Journal of the American Chemical Society 2007;129:187. [PubMed: 17199298]

30. Meyer MP, Klinman JP. Chemical Physics 2005;319:283.

31. Soudackov A, Hatcher E, Hammes-Schiffer S. Journal of Chemical Physics 2005;122:014505.

32. Hammes-Schiffer S, Soudackov AV. Journal of Physical Chemistry B 2008;112:14108.

33. Soudackov A, Hammes-Schiffer S. Journal of Chemical Physics 2000;113:2385.

34. Hatcher E, Soudackov A, Hammes-Schiffer S. Chemical Physics 2005;319:93.

35. Skone JH, Soudackov AV, Hammes-Schiffer S. Journal of the American Chemical Society 2006;128:16655. [PubMed: 17177415]

36. Georgievskii Y, Stuchebrukhov AA. Journal of Chemical Physics 2000;113:10438.

37. Kuznetsov AM, Ulstrup J. Canadian Journal of Chemistry 1999;77:1085.

38. Kohen A, Klinman JP. Accounts of Chemical Research 1998;31:397.

39. Kestner NR, Logan J, Jortner J. Journal of Physical Chemistry 1974;78:2148.

40. Bixon M, Jortner J. Advances in Chemical Physics 1999;106:35.

41. Ulstrup J, Jortner J. Journal of Chemical Physics 1975;63:4358.

42. Hammes-Schiffer S, Hatcher E, Ishikita H, Skone JH, Soudackov AV. Coordination Chemistry Reviews 2008;252:384.

43. Edwards SJ, Soudackov AV, Hammes-Schiffer S. Journal of Physical Chemistry A 2009;113:2117.

44. Dahl JP, Springborg M. Journal of Chemical Physics 1987;88:4535.

45. Meyer MP, Tomchick DR, Klinman JP. Proceedings of the National Academy of Sciences (USA) 2008;105:19562.

46. Xiang Z, Honig B. Journal of Molecular Biology 2001;311:421. [PubMed: 11478870]

47. Xiang, JZ.; Honig, B. JACKAL: A Protein Structure Modeling Package. Columbia University & Howard Hughes Medical Institute; New York: 2002.

48. Humphrey W, Dalke A, Schulten K. Journal of Molecular Graphics 1996;14:33. [PubMed: 8744570]

49. Bashford D, Karplus M. Biochemistry 1990;29:10219. [PubMed: 2271649]

50. Gordon JC, Myers JB, Folta T, Shoja V, Heath LS, Onufriev A. Nucleic Acids Res 2005;33

51. Jorgensen WL. Journal of the American Chemical Society 1981;103:335.

52. Jorgensen WL, Chandreskhar J, Madura JD, Impey RW, Klein ML. Journal of Chemical Physics 1982;79:926.

53. Cornell WD, Cieplak P, Bayly CI, Gould IR, Merz KM Jr, Ferguson DM, Spellmeyer DC, Fox T, Caldwell JW, Kollman PA. Journal of the American Chemical Society 1995;117:5179.

54. Skrzypczak-Jankun E, Bross RA, Carroll RT, Dunham WR, Funk JMO. Journal of the American Chemical Society 2001;123:10814. [PubMed: 11686682]

55. Coffa G, Schneider C, Brash AR. Biochem Biophys Res Comm 2005;338:87. [PubMed: 16111652]

56. Melchionna, S.; Cozzini, S. DLPROTEIN. 2.1. Cambridge, UK:

57. Smith, W.; Forester, TR. DL_POLY_2.14; CCLRC. Daresbury Laboratory; Warrington, England: 2003.

58. Darden T, York D, Pedersen L. Journal of Chemical Physics 1993;98:10089.

59. Ryckaert JP, Ciccotti G, Berendsen HJC. Journal of Computational Physics 1977;23:327.

60. Verlet L. Physical Review 1967;159:98.

61. Hoover WG. Physical Review A 1985;31:1695. [PubMed: 9895674]

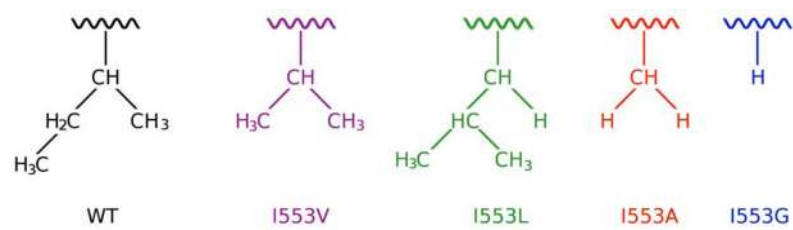62. Nose S. Molecular Physics 1984;52:255.
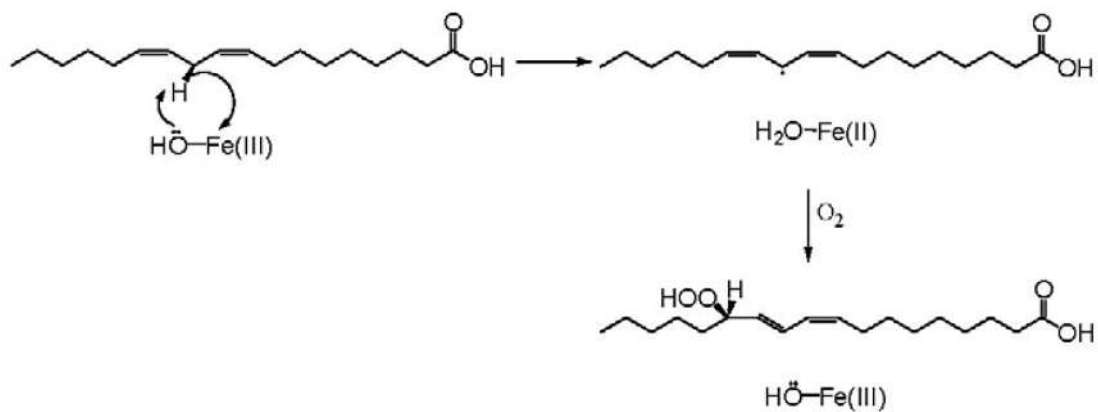
Figure 1.
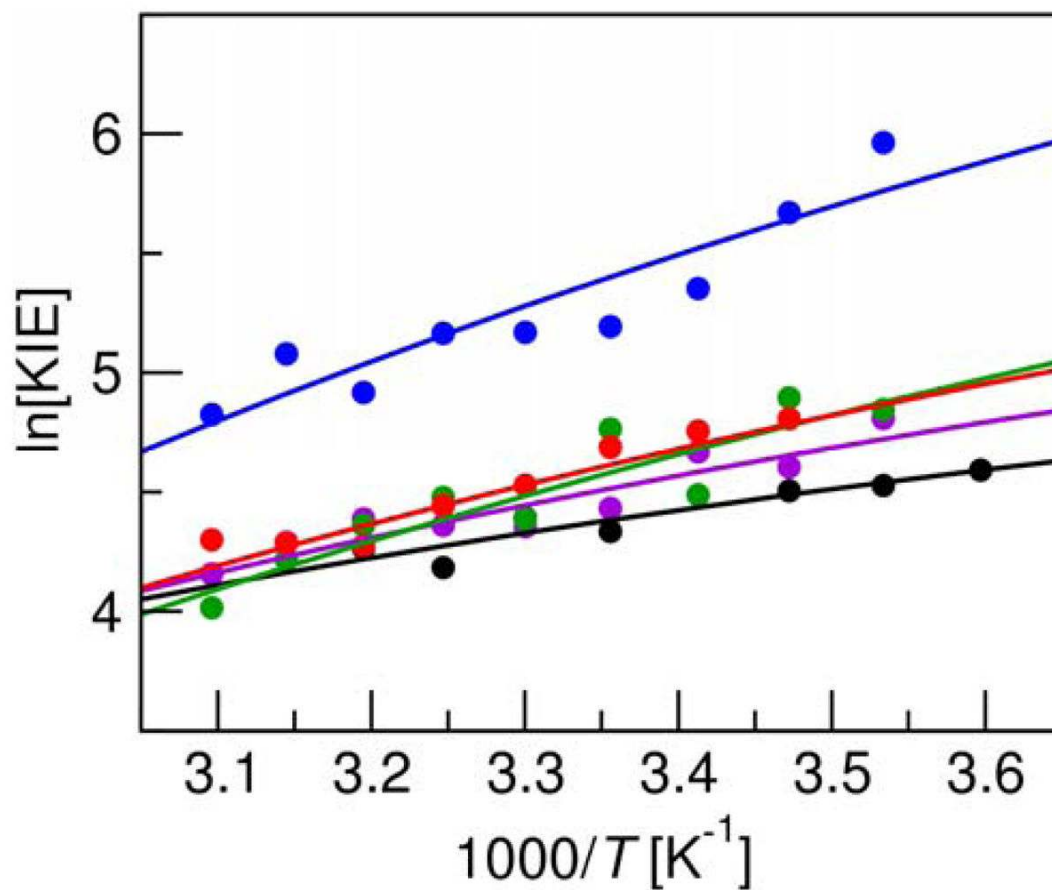Proposed mechanism of SLO. Figure reproduced with permission from Ref. [17].
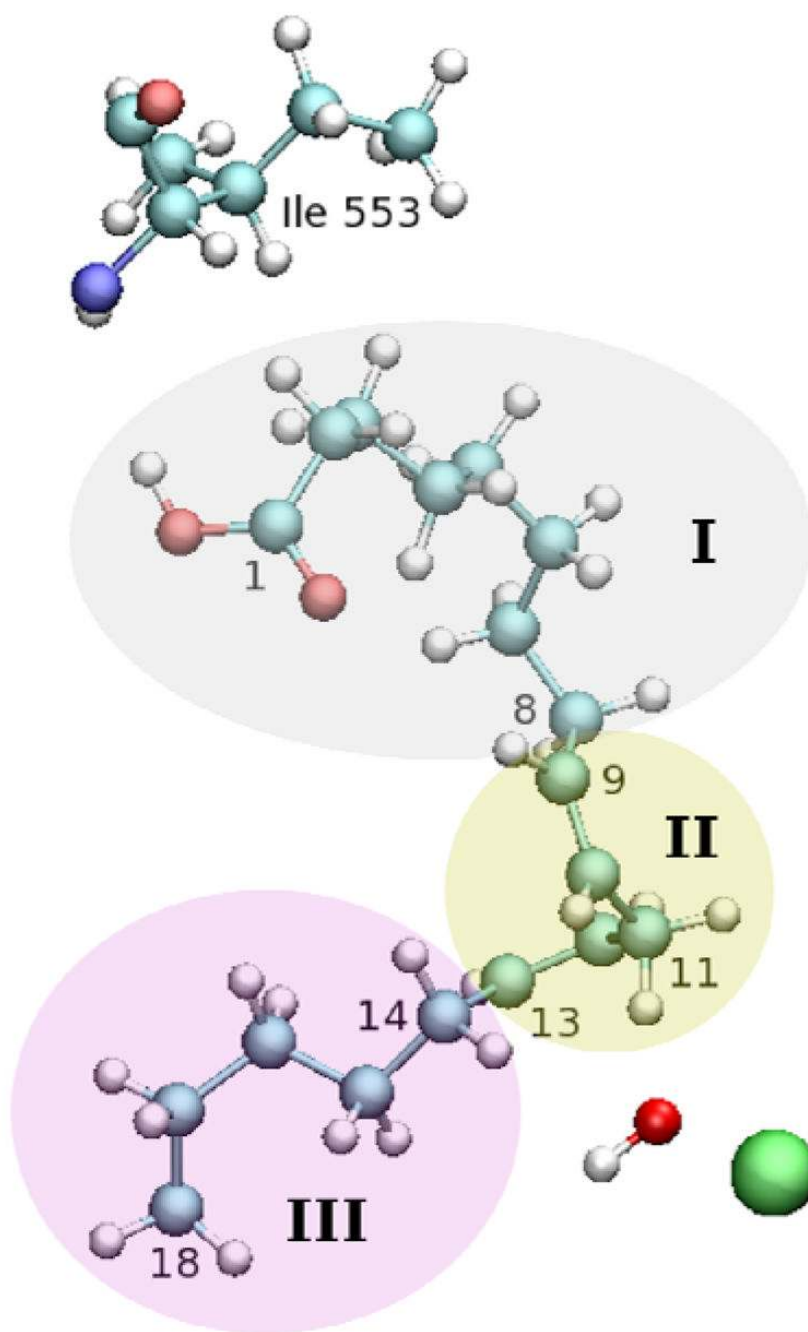
Figure 2.
Depiction of linoleic acid substrate, I553 residue, and Fe-OH portion of cofactor obtained from a snapshot of an MD trajectory. Regions I, II, and III are identified.
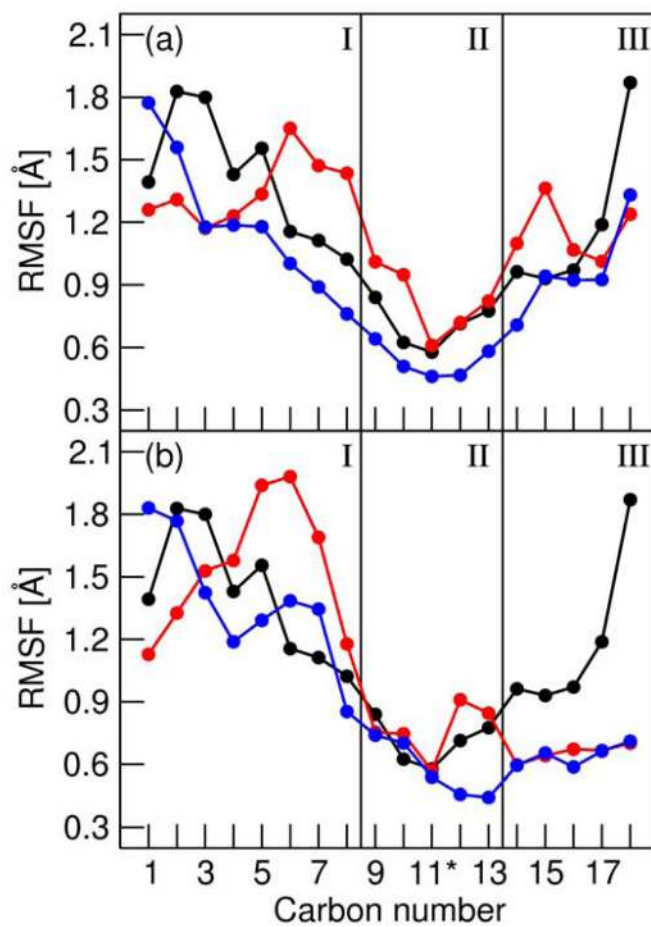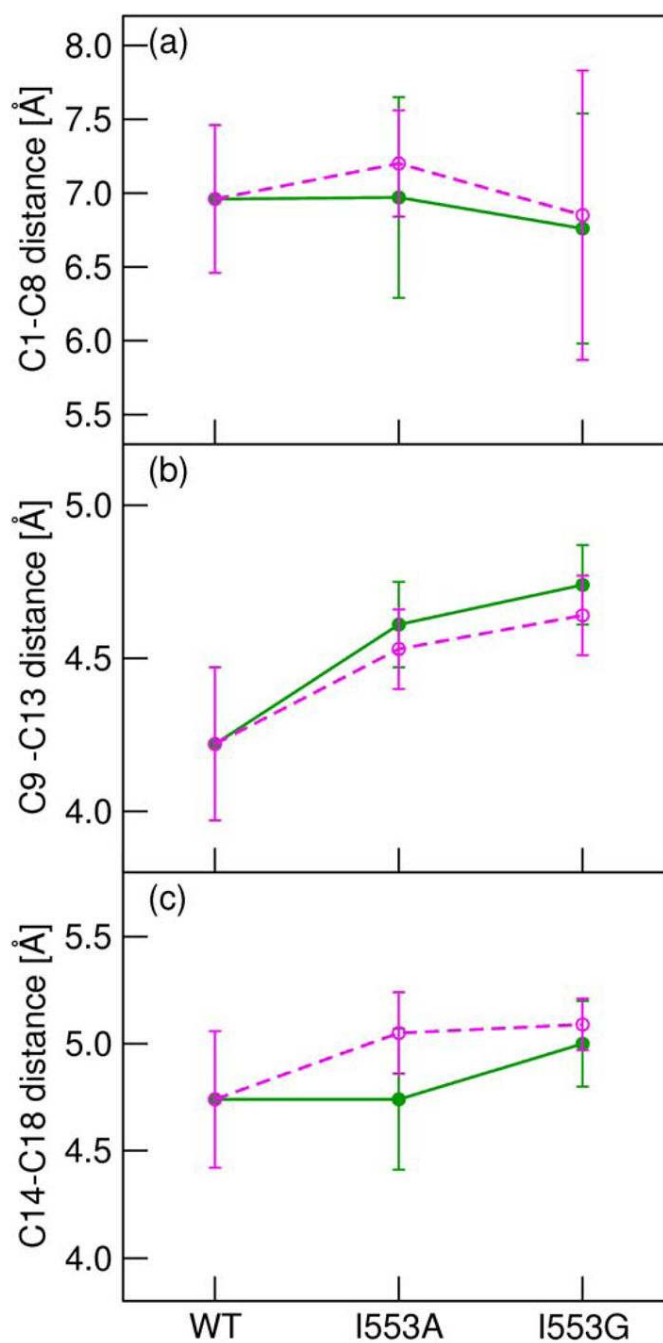
Figure 3.
Series of SLO mutants studied in the present paper. Figure modeled after scheme in Ref. [14].

Figure 4.
Plot of ln[KIE] versus 1000/T for WT SLO and the series of I553 mutants. Lines were obtained from calculations using k^{quant} with parameters given in text and Table 1. Closed circles are the experimental data from Ref. [14]. Color scheme is the same as in Figure 3: WT (black), I553V (purple), I553L (green), I553A (red), and I553G (blue).

Figure 5.
RMSF for the backbone carbon atoms in the linoleic acid substrate for WT SLO (black) and the I553A (red) and I553G (blue) mutants with (a) Structure 1 and (b) Structure 2. The lines are provided only as a visual guide.

Figure 6.
Thermally averaged distances between the backbone carbons at the ends of Regions I, II, and III of the linoleic acid substrate for WT SLO and the I553A and I553G mutants with Structure 1 (green filled circles and solid lines) and Structure 2 (magenta open circles and dashed lines). The standard deviations are indicated by vertical lines. The lines connecting the data points are provided only as a visual guide.
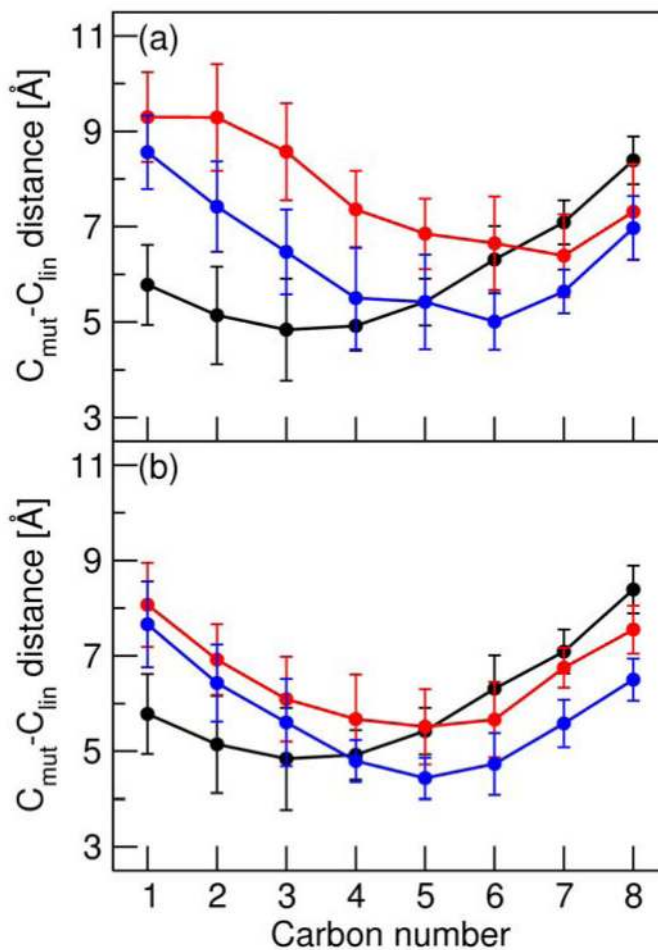
Figure 7.
Thermally averaged distances between the linoleic acid backbone carbon atoms and the α-carbon atom of residue 553 for WT SLO (black) and the I553A (red) and I553G (blue) mutants with (a) Structure 1 and (b) Structure 2. The standard deviations are indicated by vertical lines. The lines connecting the data points are provided only as a visual guide.

Table 1

Proton donor-acceptor equilibrium distances and frequencies determined for WT SLO and series of I553 mutants.[a,b]

	k^{quant}		k^{highT}	
Enzyme	$\overline{R}$	Ω	$\overline{R}$	Ω
WT	2.72	174	2.71	175
I553V	2.78	152	2.76	156
I553L	2.87	131	2.85	133
I553A	2.83	140	2.82	140
I553G	2.96	127	2.94	128

[a] $\overline{R}$ given in Å and Ω given in cm^{-1}.

[b] Fitting procedure for ln[KIE] was done with either k^{quant} from Eq. (2) or k^{highT} from Eq. (4).